Research Article

Regina Moser, Matthias Domke, Jan Winter, Heinz P. Huber* and Gerd Marowsky

Single pulse femtosecond laser ablation of silicon – a comparison between experimental and simulated two-dimensional ablation profiles

https://doi.org/10.1515/aot-2018-0013
Received February 13, 2018; accepted April 13, 2018; previously published online May 17, 2018

Abstract: Ultrashort laser pulses are widely used for the precise structuring of semiconductors like silicon (Si). We present here, for the first time, a comparative study of experimentally obtained and numerically simulated two-dimensional ablation profiles based on parameters of commercially relevant and widely used near-infrared and diode pumped femtosecond lasers. Single pulse laser ablation was studied at a center wavelength of 1040 nm and pulse duration of 380 fs (FWHM) in an irradiating fluence regime from 1 J/cm^2 to 10 J/cm^2. Process thresholds for material transport and removal were determined. Three regimes, scaling with the fluence, could be identified: low and middle fluence regimes and a hydrodynamic motion regime. By comparing the simulated and experimental ablation profiles, two conclusions can be drawn: At 2 J/cm^2, the isothermal profile of 3800 K is in excellent agreement with the observed two-dimensional ablation. Thus exceeding a temperature of 3800 K can be accepted as a simplified ablation condition at that fluence. Furthermore, we observed a distinct deviation of the experimental from the simulated ablation profiles for irradiated fluences above 4 J/cm^2. This points to hydrodynamic motion as an important contributing mechanism for laser ablation at higher fluences.

***Corresponding author: Heinz P. Huber,** Lasercenter, University of Applied Sciences Munich, Lothstrasse 34, 80335 Munich, Germany, Tel.: +49 89 1265-1686, Fax: +49 (0)89 1265-1603, e-mail: heinz.huber@hm.edu. http://orcid.org/0000-0003-2444-9833
Regina Moser and Jan Winter: Lasercenter, University of Applied Sciences Munich, Lothstrasse 34, 80335 Munich, Germany
Matthias Domke: Josef Ressel Center, Vorarlberg University of Applied Sciences, Hochschulstraße 1, 6850 Dornbirn, Austria
Gerd Marowsky: Laser-Laboratorium Göttingen e.V., Hans-Adolf-Krebs-Weg 1, 37077 Göttingen, Germany

www.degruyter.com/aot

Keywords: femtosecond laser ablation; silicon laser ablation; two-dimensional morphology; two-temperature model.

1 Introduction

The fundamental interaction between ultrafast laser radiation and silicon (Si) has been studied experimentally [1–5] and theoretically [6–8] since the 1980s in numerous works. As ultrafast lasers became commercially available in the 1990s, ultrashort laser radiation has been widely used for precise micro-processing of metals, semiconductors, and dielectrics by laser ablation [9–13]. After its absorption, the ultrashort laser radiation induces a spatially and temporally well-defined heat source, so it can be used to structure metals and semiconductors, maximize the ablation efficiency, and minimize the thermal effects on the surrounding material [9–11, 14]. This precise energy deposition is the key to damage-free cutting and microstructuring of Si, where the ablated depth is in the range of a few tens of nanometers per pulse.

The investigation of laser ablation on metal targets with pulse durations <1 ps and fluences above the ablation threshold ranging of up to 10 J/cm^2 revealed a low and a high fluence regime for the effective penetration depth of the ultrafast laser pulse energy deposition [15]. In the low fluence regime, the ablation depth was defined by an optical penetration depth, whereas in the high fluence regime, the ablation depth was associated to an effective thermal penetration depth [15]. Similar studies for Si, in this case, determined by multi-pulse laser ablation, indicated also two ablation regimes [16]. The energetic behavior of the laser ablation was studied by a determination of the damage thresholds at different pulse durations and different wavelengths in multi-pulse experiments [17, 18]. In a detailed morphological investigation, the initial modification and ablation of crystalline Si with single and multiple pulses between 5 fs and 400 fs were observed [19]. Several physical phenomena, such as oxidation,

amorphization, re-crystallization, formation of bubbles due to boiling below the surface, and ablation were reported, depending on the laser fluence and the number of pulses per position [19]. When Si surface is structured with fs-laser pulses (800 nm, 135 fs), a localized phase transformation from amorphous to crystalline phase is induced [20]. Under certain irradiation conditions, the formation of ripples, laser-induced periodic surface structures, can be observed [21–25].

Complementary to the experimental investigations, numerous theoretical studies of Si ablation with ultra-short laser pulse irradiation were performed. In metals, the classical two-temperature model (TTM) by Anisimov et al. [26, 27] described the transient temperature distribution in electron and lattice subsystems, within the non-equilibrium state. For semiconductors and dielectrics, the TTM was extended by van Driel et al. [6] by including a description of the transient optical properties during ultra-short laser excitation. Recently, this model has been further developed by taking the transient optical properties during ultrashort laser excitation into account [2, 7]. For the calculation of the melting threshold of Si as a function of the pulse duration [7, 28], the simulated values are in a good agreement with the experimental data [17, 18]. Besides surface modification and ablation, another phenomenon was expected from the simulation: a three-dimensional (3D) model including hydrodynamics at a wavelength of 800 nm in sub-ablation conditions (irradiated fluence 0.37 J/cm^2) predicted a melt propagation of liquid Si towards the crater edge forming a circular ridge outside of the ablation one, which could also be observed experimentally [21]. A further approach to model the ultra-short pulse laser interaction with Si was performed with complicated molecular dynamic (MD) simulation, which gives a detailed picture of atomic processes at the spot center. However, MD simulation indicates difficulties to calculate a two-dimensional ablation profile due to their long computation time for such a large number of atoms [29, 30].

In summarizing the state-of-the-art, the following can be stated: The ablation depth was determined only in multi-pulse experiments. Many pulses were applied at the same position under various laser pulse fluences, and the depths of the ablated craters were measured. To obtain a single pulse ablation depth, the crater depth was divided by the number of pulses [15, 16, 31]. In multi-pulse experiments, each pulse changes the optical properties of the sample and the ablation threshold decreases with the number of pulses and the repetition rate [19]. The ablation depth per pulse from multi-pulse experiments is therefore not an optimal value for a comparison with the single pulse simulations.

Combined experimental and simulation works on single-pulse laser ablation of Si use the damage thresholds determined at different pulse durations and different wavelengths in comparison to their models [7, 17, 18, 21, 28]. Damage occurs at irradiated fluences of about 0.1 J/cm^2–0.3 J/cm^2. However, for laser materials processing, which would be relevant for industrial applications, a comparison at one order of magnitude higher laser fluences would be interesting, where ablation efficiency in terms of irradiated energy divided by the ablation volume has an optimum [32, 33].

Therefore, in this work, two-dimensional ablation profiles were also measured, not only the ablation depths in single pulse experiments at fluences between 1 J/cm^2 and 10 J/cm^2 where ablation efficiency is reaching its optimum [33]. As the laser source, a diode-pumped near-infrared laser with 1040-nm center wavelength and 380-fs pulse duration (FWHM) was used, as applied in 1000 s of units for medical and industrial applications, such as eye surgery, stent, and glass cutting, which exhibited a center wavelength of 1040 nm and FWHM pulse duration of 380 fs. Furthermore, a simple thermal TTM was applied to simulate the transient temperature distribution in a Si substrate following the ultrashort laser irradiation. After the electron and lattice temperatures reached equilibrium, the two-dimensional temperatures profiles were calculated and compared with experimental two-dimensional single pulse laser ablation profiles in Si.

2 Materials and methods

2.1 Experiment

The experimental investigations were performed on a monocrystalline Si wafer (p-type, <100>) with a diameter of 100 mm and thickness 525 µm. P-type silicon is usually used in semiconductor and solar cell manufacturing as substrate material.

The laser processing machine (microSTRUCT vario, 3D-Micromac, Chemnitz, Germany) housed an ultrafast laser source (Spirit, Spectra-Physics, Rankweil, Austria) with a pulse duration of about 380 fs (FWHM). The laser was operated at 1040 nm. The focal length of the focusing optic was 100 mm. The focus radius was determined as $w_0 = 9.7$ µm (at an intensity of $1/e^2$) using the D^2-method [34], where the relation between ablated radius and pulse energy was used to accurately determine the laser ablation threshold fluence and the beam diameter in the focus. The material used for the determination of the focus diameter was Al, as Si exhibits nonlinear behavior, as discussed in this study. The maximum available pulse energy was $E = 20.5$ µJ. A maximum peak fluence F_0 of up to 13.9 J/cm^2 could be applied. Lower peak fluences were adjusted with a combination of a half wave plate and a polarizer. All fluence values given in this study correspond to the peak values of the Gaussian beam profiles.

In this study, single pulse laser ablation of the Si sample was performed across a range of laser fluences. For each new fluence, a new sample surface was presented by shifting the distance between each of the pulses by 50 µm. The fluence was gradually decreased until the different process thresholds were reached. The 3D surface profile was measured with a confocal microscope (µsurf, NanoFocus, Oberhausen, Germany) with a depth spatial resolution of approximately 5 nm. In addition, the topographic morphology of the ablated spots was investigated by a scanning electron microscope (7100F, JEOL, Eching, Germany).

2.2 Theoretical model

During ultra-short pulse laser irradiation, the electron and lattice systems are in non-equilibrium. Assuming that the electronic relaxation times are small compared to the laser pulse duration, the energy transfer inside the material can be described by the well-known TTM until a thermodynamic equilibrium between electron and lattice system is reached [26, 27]. The TTM is mathematically written as coupled non-linear differential equations for the electron and lattice subsystems.

The ultrashort lasers pulses excite electron-hole pairs (charge carriers) in semiconductors, whose energy is then transferred to the lattice by scattering processes. At first, Van Driel [6] proposed a theory for the electron-hole pair balance equation to determine the carrier density, carrier energy, and lattice energy derived from a relaxation time approximation of the Boltzmann's transport equation.

2.2.1 Laser pulse absorption: The ultrashort laser pulse is mathematically defined as a heat source with spatial and temporal form of an ideal Gaussian, which is shown in Eq. (1). The intensity, $I(z=0, t)$ of the laser pulse at the Si surface is obtained by

$$I(z=0,\ t)=\sqrt{\frac{4\ln(2)}{\pi}}\frac{(1-R)F_0}{t_p}\cdot\exp\left(\frac{2r^2}{{w_0}^2}\right)\cdot\exp\left[-4\ln(2)\left(\frac{t}{\tau_p}\right)^2\right], \tag{1}$$

where R represents the initial surface reflectivity; F_0, the laser fluence; τ_p, the FWHM pulse duration; r, the radius perpendicular to the beam direction; t, the time variable; and w_0, the beam radius at an intensity level of $1/e^2$.

In contrast to metals, where the laser pulse energy is absorbed typically by the inverse bremsstrahlung of free electrons in the conduction band, the conduction band of semiconductors is nearly empty. In semiconductors, the laser pulse energy absorption is mainly determined by the interband absorption of the bounded electrons from the valence band with major contribution of single- and two-photon interband absorptions. In Si, the primary form of photon absorption is through indirect processes, where momentum conservation takes place through phonon emission or absorption in the conduction band. In addition, electrons in the conduction band can further absorb the laser pulse energy by inverse bremsstrahlung similar to metals where this process is known as free carrier absorption (FCA) [7]. Reintjes and McGroddy [35] experimentally observed the non-linear indirect two-photon absorption (TPA) in Si as a stepwise optical absorption processes involving interband and intraband free carrier absorption. Electrons with a high kinetic energy can also trigger a further process, known as impact ionization. In this process, an electron in the conduction band gains energy from FCA and it can create a further electron-hole pair by exciting an electron from the valence band to the conduction band. Generally, in Si, conduction band electrons are generated by linear absorption, non-linear TPA, and impact ionization, whereby electrons are removed through Auger recombination.

The laser pulse attenuation within the material in the direction of the pulse propagation is solved by one-dimensional ordinary differential equation (ODE) for each spatial domain within the 3D simulation. The ODE describes the spatial evolution of the intensity inside the material and can be expressed as the following equation, similar to those in Ref. [7]:

$$\frac{\partial I(z,\ t,\ r)}{\partial z}=-(\alpha_{\mathrm{SPA}}+\alpha_{\mathrm{FCA}})I-\beta_{\mathrm{TPA}}\ I^2. \tag{2}$$

This equation explicitly computes the temporal and spatial intensity distribution in the material at different spatial depths z. It includes the single-photon absorption (SPA) coefficient α_{SPA}, the FCA coefficient α_{SPA}, the free carrier absorption (FCA) coefficient $\alpha_{\mathrm{FCA}}=\theta N$ [36] with the cross-section θ, the TPA coefficient β_{TPA}, and the material carrier number density N. In the limit of $\theta=0$ and $\beta_{\mathrm{TPA}}=0$, Eqs. (1) und (2) lead to the general expression of the Lambert-Beer law [36]. In summary, the total source term including all laser absorption mechanisms is written by

$$S(z,\ t,\ r)=\alpha_{\mathrm{tot}}I(z,\ t,\ r)=\frac{\partial I(z,\ t,\ r)}{\partial z}. \tag{3}$$

Here α_{tot} is the collective term including all absorption coefficients, and I is the intensity at the depth z depending on the absorption coefficient between the surface and the position z.

The linear FCA coefficient α_{FCA} in the heat source term includes the temperature dependency of the cross-section and depends also on the carrier density. This dependence leads to significant changes in the optical properties of a semiconductor. In the following, a Drude model was used to calculate change of the complex dielectric function of laser excited Si, taking into account the temperature and carrier dependency during the ultrashort laser radiation [21]. The complex transient dielectric function dependence on the of laser frequency ω_L is given by

$$\epsilon_{\mathrm{Si}}(\omega_L)=\epsilon'(\omega_L)+i\epsilon''(\omega_L)=\epsilon_r-\frac{\omega_p^2}{\omega_L^2+i\omega_L\nu}, \tag{4}$$

where ϵ_r is the intrinsic dielectric constant; ν, the Drude collision frequency of electrons; and ω_p, the plasma frequency. The plasma frequency is defined as $\omega_P^2=\frac{Ne^2}{\epsilon_r\epsilon_0 m_{\mathrm{eff}}}$ with the intrinsic dielectric function ϵ_r, electron charge e effective electron mass m_{eff}, and N as carrier density of free electrons in the conduction band [7, 17, 18, 21, 28, 36].

From the complex dielectric function, the complex refractive index $\tilde{N}=\sqrt{\epsilon_{\mathrm{Si}}}=(n-ik)^2$ can be derived. The real part of $\tilde{N}$ is given by the refractive index n, and the imaginary part, by the extinction coefficient k. Using the relations $\epsilon'=n^2-k^2$ and $\epsilon''=2nk$, the real and imaginary parts of the complex refractive index can be expressed in relation to the real and imaginary parts of the dielectric function ϵ' and ϵ''

$$n=\sqrt{\frac{\sqrt{\epsilon'^2+\epsilon''^2}+\epsilon'}{2}},\quad\text{and} \tag{5}$$

$$k=\sqrt{\frac{\sqrt{\epsilon'^2+\epsilon''^2}-\epsilon'}{2}}. \quad (6)$$

The reflectivity R under normal incidence and linear free FCA α_{FCA} can be calculated from the Fresnel equation according to

$$R=\frac{(n-1)^2+k^2}{(n+1)^2+k^2}. \quad (7)$$

In Eq. (2), the laser pulse absorption within the material includes the linear absorption, the free carrier absorption (FCA), and the TPA mechanisms and is summarized to the total absorption term in Eq. (3). However, the linear absorption in this total absorption term can be calculated directly from the imaginary part of the dielectric function. The liner absorption is described by linear free carrier absorption coefficient α_{FCA} and is given as

$$\alpha_{FCA}=\frac{2\omega_L k}{c_0}, \quad (8)$$

where c_0 denotes the speed of light in vacuum [37].

2.2.2 Energy and free-carrier dynamics: For the carrier balance equation, the carrier number density N in the conduction band was calculated considering one-photon absorption and TPA, carrier diffusion, impact ionization, and Auger recombination. The temporal evolution of the carrier number density change is calculated according to Eq. (9) by solving a partial differential equation as reported in Ref. [7].

$$\frac{\partial N}{\partial t}=\nabla(D_0\nabla N)-\gamma(T_e)N^3+\delta(T_e)N+\frac{\alpha_{SPA}I}{\hbar\omega_L}+\frac{\beta_{TPA}I^2}{2\hbar\omega_L} \quad (9)$$

Here D_0 is the ambipolar diffusivity; γ, the Auger recombination coefficient; δ, the impact ionization coefficient depending on the electron temperature T_e, and $\hbar\omega_L$, the photon energy [16].

The self-consistent model for energetic transport dynamics in semiconductors is based on the relaxation time approximation of the Boltzmann transport equation. The free carrier densities of electrons in the conduction band and in the lattice in the non-equilibrium state are described in the temporal and spatial evolution of the carrier density and temperature as well as the lattice temperature in the framework of the TTM [7, 28, 36, 38]. The balance equation for carrier energy density dynamic for the electron-hole pairs is written as

$$3Nk_B\frac{\partial T_e}{\partial t}=\nabla\cdot(k_e\nabla T_e)-G(T_e-T_l)+S-\frac{\partial N}{\partial t}(E_g+3k_BT_e)-N\left(\frac{\partial E_g}{\partial N}\frac{\partial N}{\partial t}+\frac{\partial E_g}{\partial T_l}\frac{\partial T_l}{\partial t}\right), \quad (10)$$

where N is the density of free electrons; k_B, the Boltzmann constant; and k_e, the electronic heat conduction. G is the electron-phonon coupling dependence on the free electron density and is given in the form $G=3Nk_B/\tau_e$, whereby τ_e is the carrier-lattice relaxation time. The fundamental band gap energy E_g is assumed to be dependent on the lattice temperature [36].

Also, the balance equation for lattice energy density described by the lattice thermal conduction equation is expressed in well-known form by

$$C_l\frac{\partial T_l}{\partial t}=\nabla\cdot(k_l\nabla N)+G(T_e-T_l), \quad (11)$$

where C_l is the heat capacity of the lattice.

The phase transition from solid to liquid and from liquid to vapor occurs when the equilibrium temperature for melting and evaporation is reached and sufficient energy can be supplied to overcome the latent heat of melting evaporation. The lattice temperature-dependent heat capacities are simulated in the model by using a suitable representation, which consists of a Gaussian distribution function with a finite width ΔT centered on the melting temperature T_m and the evaporation temperature T_v [21]. This results in a smoother transition between solid and liquid phase transitions during the simulated material heating [39].

This simulated evaporation process is used as the condition to determine the material ejection during laser heating. Table 1 gives a full summary of the material parameters used during the simulations.

Table 1: Model parameters of Si used for the simulations in this work [6].

Parameter	Symbol	Value
Lattice thermal conductivity [38]	k_l	$1.585^{1.23}\cdot T_l^{-1.23}$ (W/(cm³K))
Evaporation temperature	T_v	3583 (K)
Melting temperature	T_m	1687 (K)
Carrier ambipolar diffusivity [38]	D_0	$18\cdot\frac{300\text{ K}}{T_l}$ (cm²/s)
Auger recombination coefficient [36]	γ	3.8×10^{-31} (cm⁶/s)
Impact ionization coefficient [36]	δ	$3.6\times10^{10}\cdot e^{-\frac{1.5E_g}{k_B\cdot T_e}}$ (1/s)
Carrier-phonon relaxation time [36]	τ_{e-l}	$240\cdot\frac{(1+N)}{6\cdot10^{20}}$ (fs)
Two photon absorption	β	9 (cm/GW)
Free carrier absorption-cross section [38]	θ	$5.1\times10^{10}\cdot\frac{T_l}{300\text{ K}}$(cm²)
Electronic heat capacity [38]	C_{pe}	$3\cdot N\cdot k_B$ (J/k/m³)
Heat capacity of lattice [38]	C_l	$\left(1.978+3.54\cdot10^{-4}\cdot T_l-\frac{3.68}{T_l^2}\right)-1.978\cdot10^6+4.19\times10^9\frac{1}{\sqrt{2\cdot\pi}\cdot100}\cdot e^{-0.5\frac{T_l}{100}}$ (J/k/m³)

3 Results and discussion

3.1 Single pulse laser ablation of silicon and its morphology

In Figure 1, the topographic morphology of the laser irradiated Si is shown over a wide laser fluence range from 0.25 to 10.3 J/cm^2. The observed morphology was divided into low and middle fluence regime. A third new fluence regime appears at fluences above 4 J/cm^2, which is connected with the hydrodynamic motion of molten silicon.

In the low fluence regime (see Figure 1; 0.25, 0.5 and 0.78 J/cm^2), the modified Si surface features two areas, a darker part in the center surrounded by a bright ring. In addition, a dark ring with a 5-µm diameter is detectable at fluences of 0.5 and 0.78 J/cm^2. Bonse et al. [19] described different areas inside the laser interaction zone caused by ablation and melting (in the center), surrounded by a modification zone caused by oxidation/amorphization. The bright ring observed in the SEM images at fluences 0.25 J/cm^2–2 J/cm^2 is considered to be an artifact of the SEM. In the low fluence regime, the dark circular area can be identified as the melt region and subsequent re-solidification zone. The dark ring observed at the edge of the irradiated silicon for the higher fluences of 0.5 J/cm^2 and 0.78 J/cm^2 is due to propagation of the thin melt front and re-solidification after melting. In the central part of the crater, no significant ablation depth can be measured at fluences between 0.25 J/cm^2 and 0.5 J/cm^2 (see Figure 1, 0.25 and 0.5 J/cm^2) within the spatial resolution of the confocal microscopy of about 5 nm. As the fluence is increased to 1 J/cm^2, the material removal process begins, and an ablation depth of ~20 nm is observed. However, well-defined ablation diameters could not be measured by confocal microscopy at this fluence. The ablation radius and depth can be accurately measured above a fluence of approximately 1 J/cm^2; both are shown in Figures 2 and 3. The theoretical ablation threshold can also be determined using the typical D^2-method as well as using the ablation depth method. In both cases, the ablation threshold is determined by the interception of the regression curve with the abscissa at a fluence of approximately 0.7 J/cm^2, as shown in Figures 2 and 3. Thus, the low fluence regime can be related to the optical breakdown and damage regime reported by previous works [17, 18]. Several groups have connected the damage threshold to the appearance of a luminous plasma. This optical breakdown at the damage threshold is related to a dense free-electron plasma close to the critical electron density of 1×10^{21} cm^3 for the used laser wavelength. This is followed by a thermophysical heating of the underlying material through electron-ion scattering [17, 18]. In summary, the low fluence regime displays mainly no ablation but indicates the surface modification initiated by optical breakdown and the dynamics of liquid silicon until re-solidification leads to a circular dark ring.

The middle fluence regime displays the laser ablation of Si in the fluence range from 2 to 4 J/cm^2 (Figure 1). The ablation depth for single pulse irradiation increases from about 50 nm at 2 J/cm^2, 100 nm at 3 J/cm^2 to 150 nm at 4 J/cm^2 (Figure 3). The surface roughness (peak to peak) of the laser processed area can be estimated to be in

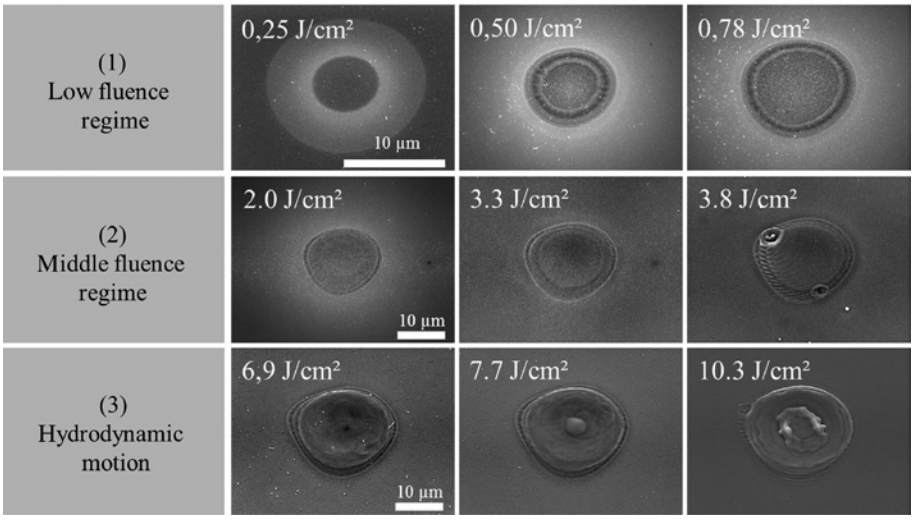

Figure 1: Ablation morphology of single pulse laser ablated Si for a wavelength of 1040 nm and a pulse duration of 380 fs at different fluences (from 0.25 J/cm^2 up to 10.3 J/cm^2) recorded with by scanning electron microscopy and divided into three different regimes: a low fluence, a middle fluence, and a hydrodynamic motion regime.

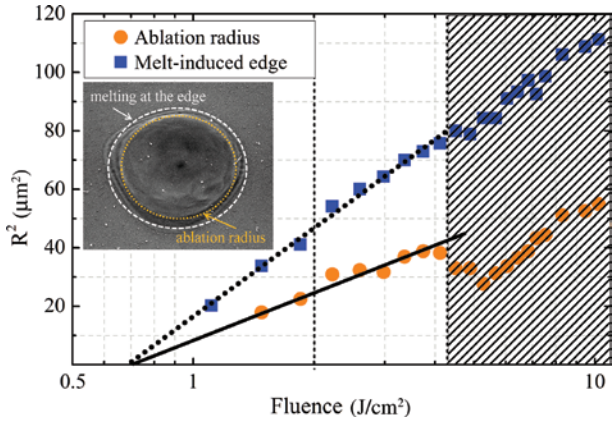

Figure 2: Determination of the threshold fluence according to the D²-method. The ablation radius is shown with black points and the melt-induced edge radius is indicated with blue squares.

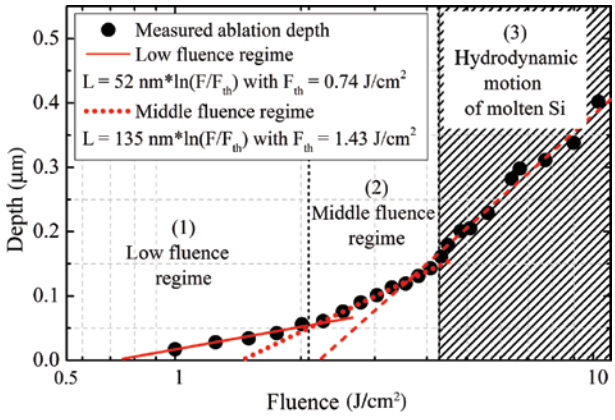

Figure 3: Comparison between the measured ablated crater depths (black circles) for the different fluences in a semi-logarithmic plot. The depth values were fit assuming a Lambert-Beer-like absorption or energy deposition with a linear function yielding a penetration depth of 52 nm and 135 nm.

the order of 10 nm. At applied fluences of 3.3 J/cm² and 3.8 J/cm², the circular burr outside the ablation zone has measured heights of 20 nm and 50 nm, respectively. This indicates the beginning of significant hydrodynamic motion of liquid silicon from the crater center to the edge (here called melt-induced edge).

A further, third fluence regime of hydrodynamic motion of the molten silicon followed by re-solidification on the edge was identified at higher fluences from 4 J/cm² to 10 J/cm² (Figure 3). In this regime, the ablation depth increases from 150 nm to 350 nm as a function of the laser fluence. The ablation diameter initially increases up to a fluence of 4 J/cm² to a value ~13 µm. This is followed by a decrease in ablation diameter to values of ~10 µm for higher fluences in the range of 4 J/cm²–5.5 J/cm², while the ablation depth is continually growing (as shown in Figures 2 and 3). At fluences of 7.7 J/cm²–10.3 J/cm² (Figure 1), the material motion of molten silicon towards the edge is occurring in the central part of the irradiated zone. The experimental observation in Figure 1 in the third fluence regime can be described as a motion of molten Si followed by a solidification process, after the lattice temperature is cooled down below the melting point. According to Tsibidis et al. [21], the hydrodynamic motion of molten silicon is mainly influenced by recoil pressure. The exponential dependence of the recoil pressure on the temperature induces a large radial temperature gradient and, in following, is responsible for the melt flow in the radial direction. This produces a melt ejection towards the edge of the irradiated zone. Finally, the flow of molten Si towards the edge with following re-solidification reduces the ablation diameter and is forming a circular ridge around the ablation zone, which is indicated in Figure 1 as melt-induced edge.

3.2 Determination of process thresholds in single-pulse experiments

Two different laser-initiated processes could be identified and connect with a measureable diameter: a melt-induced edge due to hydrodynamic motion of molten silicon and re-solidification at the edge and the ablation zone in the central part with a smaller diameter.

The threshold behavior of the silicon sample under femtosecond laser irradiation was determined by confocal microscopy of the laser ablation, at fluences from about 1 J/cm to 10 J/cm², as described in section 3.1 and using the well-known D²-method [34]. Two separate material features can be observed, namely, the melt-induced edge and the ablation zone. The process related to the melt-induced edge exhibits a threshold fluence of 0.69 J/cm² with an effective radius of 13.3 µm. For the ablation process, a threshold fluence of 0.70 J/cm² is determined with an effective radius of 9.5 µm, as shown in Figure 2. The thresholds measurement uncertainty is estimated at 5%. Thus, the threshold fluences for both processes can be assumed to be equal within the uncertainties of the measurements. However, the effective radii of both processes obtained from the regression curve differ significantly. It is known from literature that the effective beam radius should be in reasonably good agreement with the optical beam radius. The optical beam radius was measured with direct laser ablation on reference Al samples using the D²-method. This beam radius of 9.7 µm (section 3.1) is in good agreement with the determined effective ablation radius of 9.5 µm for ablation (Table 2). The melt-induced

Table 2: Single pulse laser thresholds and effective beam radius of Si at 1040-nm wavelength and 380-fs pulse duration for ablation and melt-induced edge.

Laser initiated process	Threshold fluence (J/cm²)	Effective beam radius (μm)
Ablation	0.70	9.5
Melt-induced edge	0.69	13.3

edge radius of 13.3 μm (Table 2), however, indicates a significant deviation in the slope and thus a change from the optical beam radius.

The threshold measurement method is based mainly on two assumptions, an ideal Gaussian beam and an ideal threshold behavior. The observed ablation process occurs at a local point in the sample plane, where the Gaussian fluence distribution (energy density in J/cm²) locally exceeds the threshold fluence; this further implies that below threshold, the process does not occur. Obviously, the laser pulse irradiation with the optical beam radius of 9.7 μm induces a melt-induced edge process with a much larger radius of 13.3 μm. This fact may be the result of a hydrodynamic transport process, where molten Si material is pushed outside the laser beam center and re-solidified. This leads to a process radius significantly larger than the optical beam radius and to a deviation of the slope in measured radii. Thus, a deviation of optical and effective beam radii may point to a transport process violating the locality assumption of the threshold method. Indeed, a significant melt front shift is observed for the Si ablation beginning in the middle fluence above about 3.3 J/cm² and in the hydrodynamic motion regime (Figure 1). Thus, a deviation of optical and effective beam radii may point to a transport process violating the locality assumption of the threshold method. Indeed, a significant material motion is observed for the Si ablation in the central part at fluence above 3 J/cm² and in the hydrodynamic motion regime (Figure 1).

3.3 Ablation depths in different fluence regimes

The evolution of the ablation depth from low to high laser fluence in comparison with the experimental measurement (black dots) by an optical confocal microscopy method is shown in Figure 3.

A logarithmical fit to the experimental data in low fluence regime (<2 J/cm²) gives a threshold fluence of $F_{th} = 0.74$ J/cm² and an effective penetration depth of 52 nm (Figure 3). In the middle fluence regime (~2–4 J/cm²), the fit values are determined to be 1.43 J/cm² and 135 nm, respectively. Two ablation regimes were associated in literature with two different logarithmic dependences, one due to the optical penetration and another due to electron heat diffusion [15]. In the low fluence regime, the slope of the fit function can be associated with the skin depth of a plasma at critical density leading to an optical penetration depth of 52 nm. The middle fluence regime (2–4 J/cm²) is characterized by electronic heat conduction, driven by a high electron temperature gradient in the material, with an effective penetration depth of 135 nm. Following reference [15], the effective penetration depth results from an integration over the laser heat source processes due to optical absorption (linear, two-photon, and free carrier absorption, as described in section 3.2.1) and heat diffusion processes. In addition, a third regime associated with the hydrodynamic motion of molten Si material can be identified for fluences >4 J/cm².

3.4 Simulated and measured ablation profiles in the middle fluence regime

Figure 4 illustrates the comparison of the measured ablation profile (black solid curve) and the simulated lattice temperature fields after the electron and lattice temperatures have reached equilibrium in the middle fluence regime. The temperature field is depicted in terms of isothermal profiles at different lattice temperatures. The red dashed line gives the isothermal for evaporation temperature of 3538 K.

In the low fluence regime for fluences <1 J/cm², only a surface modification is observed, as also reported in other previous works [17–19]. In this fluence range, the calculated temperature evolution around the silicon melting temperature of 1687 K was achieved (data not shown here).

At a fluence of 1 J/cm, an ablation depth of 20 nm was measured (Figure 3). At that fluence, no noticeable melt-induced edge around the ablation crater is detected. The simulated temperature at the surface exceeds the evaporation temperature of 3583 K and the two-dimensional isothermal contour at evaporation temperature exhibits also a maximum depth of 20 nm. It follows coarsely the measured ablation profile, but the ablation diameter is a few μm wider than the simulated one (data not shown here).

As the laser fluence is increased up to 2.0 J/cm², entering the middle fluence regime, the ablation crater becomes deeper and extends to about 50 nm (Figures 3 and 4 at 2.0 J/cm²). The ablation area still shows no burr surrounding the crater geometry. The simulated

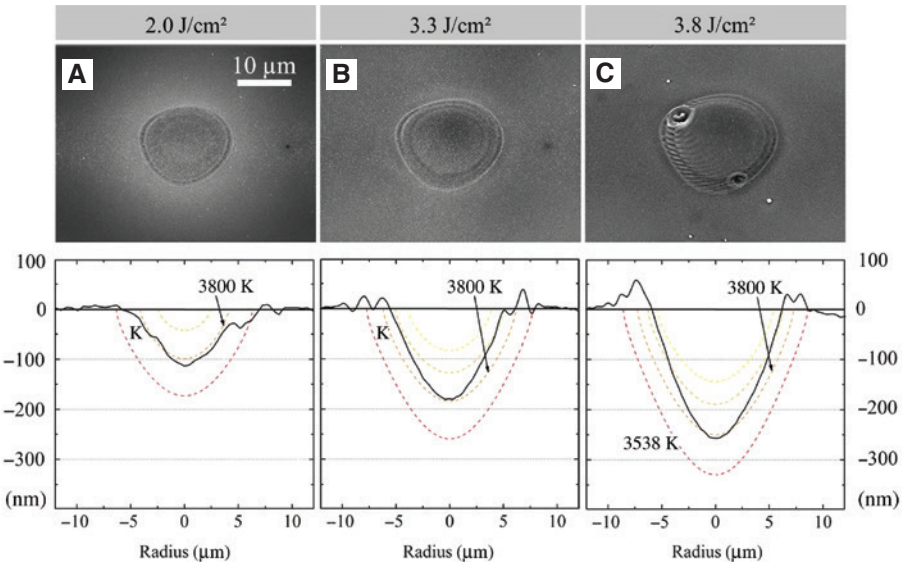

Figure 4: Comparison between the ablation profiles of Si at a wavelength of 1040 nm (black solid line) and the simulated isothermal profiles for different fluences at 2 J/cm² in (A), 3.3 J/cm² in (B), and 3.8 J/cm² in (C). The isothermals are given in dashed lines at different colors. Evaporation temperature at 3583 K is in red dashes; higher temperatures of 3800 K, in orange; and 4000 K, in dark yellow and 6000 K, in bright yellow.

isothermal profile at evaporation temperature exhibits a parabolic geometry. But now the measured ablation geometry corresponds very well with the simulated temperature isotherm of 3800 K and not the evaporation temperature of 3583 K.

At 3.3 J/cm², the ablation morphology continues to extend in depth and begins to show a burr formed by melt around the ablation zone with a height of 10 nm–20 nm (see Figures 3 and 4 at 3.0 J/cm²). The ablation depth matches the depth of the 3800 K isotherm contour exactly. The ablation diameter, however, does not increase as expected from the 3800 K isothermal curve but is increasing disproportional and is now in good agreement with the simulated isotherm of 4000 K (see Figure 4, 3.0 J/cm², dark yellow dashes). The aspect ratio defined by the ablation depth divided by the ablation radius increases.

An explicit burr around the ablation crater with a height of 20 nm–30 nm develops at a fluence exceeding 3.8 J/cm². The geometry difference of the 3800 K isotherm and the measured ablation crater becomes more significant. The ablation depth is still very close to the simulated depth of 3800 K, and the ablation radius corresponds to the simulated isothermal curve at 4000 K or even a little bit higher (see Figure 4 for 3.0 J/cm², orange and dark yellow dashes). The ablation geometry at fluence of 3.8 J/cm² (see Figure 4C) extends more in the depth dimension and less in the radial dimension; the aspect ratio is further enlarged.

For 5 J/cm² in the hydrodynamic motion regime, a growing aspect ratio and an increasing deviation of the measured ablation profile from the simulated isotherms are observed. A melt-induced edge surrounding the ablated crater can be clearly recognized. The ablation is deeper (at evaporation isotherm contour) and has a smaller radius (corresponds to 6000 K isotherm contour) than the simulated 3800 K isotherm (data not shown here).

In summary, a few interesting observations can be noted here:

In the middle fluence regime and especially at 2 J/cm², the simulated 3800 K isotherm contour exhibits a very high similarity in shape and size. Thus the transgression of temperatures over 3800 K seems to be a good and simplified ablation condition for predicting the ablation morphology accurately. The deviation between simulated and measured depth is less than 5 nm. For an industrial application, our simple optical and thermal model might be sufficient to predict the ablation dimensions for a subtractive materials processing in the single pulse domain, where multi-pulse effects such as heat accumulation and change of absorption for successive pulse can be neglected.

For higher fluences, the ablation aspect ratio grows, so that the two-dimensional ablation morphology differs from the shape of the 3800 K isotherm contour. In the middle fluence regime, still the ablation depth is predicted by the 3800-K isotherm contour; the ablation width, however, rather corresponds to the narrower 4000-K isotherm contour. In the hydrodynamic motion regime, ablation aspect, two-dimensional shape, and dimensions exceed the morphology predicted by isothermal curves. Thus here, the observation contradicts the predictions of

our simple theory and no longer supports the transgression of the 3800-K isotherm as a valid ablation criterion. This can be well understood, as features of hydrodynamic motion of liquid silicon from the ablation center to the rim are observed in the D^2-method, ablation depth measurements, and the comparison of two-dimensional ablation profiles with the isothermal lines (Figures 2–4) but are not included in the simple optical and temperature modelling of our simulations here. Thus the deviation from experiments and model gives rise to the conclusion that hydrodynamic motion is necessary to understand the behavior of the fs laser ablation of silicon with single pulses at higher fluences than about 4 J/cm^2 [21].

4 Conclusions

In this work, for the first time, an industrial diode-pumped, near-infrared femtosecond laser at 1040 nm and 380 fs was used for single pulse ablation experiments in Si. Two-dimensional ablation profiles of the ablated spots were compared to two-dimensional isothermal contours from a simple optical and thermal simulation.

The laser ablation process can be described in terms of a very simplified thermal ablation model in the middle fluence regime. The simulation in this work leads to nearly parabolic isothermal surfaces of the Si lattice temperature. From 1 J/cm^2 up to 3.8 J/cm^2, which includes the middle fluence regime, the experimentally determined ablation profiles show good agreement with the 3800-K isothermal contours. These results verify the assumption that reaching a temperature of 3800 K in the Si lattice system, which lies just about 6% above the evaporation temperature of 3583 K, is a very simple and sufficiently good ablation condition for the simulation of the direct laser ablation of Si with femtosecond laser pulses. In the middle fluence regime, the ablation is dominated by optical energy deposition and heat diffusion leading to optimized efficiency and surface quality.

In the high fluence regime, a deviation from our model and experimental measurements is observed, as hydrodynamic effects such as melt propagation, which are missing in the model, come into play. Thus melt propagation is the effect that dominates the high fluence regime.

Whereas the middle fluence regime exhibits thermal ablation, the high fluence regime displays a significant component of motion of liquid silicon. The studies of the work at hand close a research gap by combining both experiments and simulations on femtosecond laser ablation of Si with industrial relevant laser parameters.

Acknowledgments: This work was partly funded by the Bundesministerium für Wirtschaft und Energie (BMWi) in the project MONOSCRIBE (grant no. 0325922A) and by the DFG in grant no. HU1893/2-1. Support by Spectra Physics Austria is further acknowledged for close collaboration and financial support of the Josef Ressel Centre for material processing with ultrashort pulsed lasers. The financial support by the Austrian Federal Ministry of Economy, Family and Youth and the National Foundation for Research, Technology and Development is gratefully acknowledged.

References

[1] M. C. Downer, R. L. Fork and C. V. Shank, J. Opt. Soc. Am. A Optics Image Sci. Vision. 2, 595–599 (1985).
[2] C. V. Shank, Phys. Rev. Lett. 51, 900–902 (1983).
[3] C. V. Shank, R. Yen and C. Hirlimann, Phys. Rev. Lett. 50, 454–457 (1983).
[4] A. Cavalleri, K. Sokolowski-tinten, J. Bialkowski, M. Schreiner and D. Von Der Linde. J. Appl. Phys. 85, 3301 (1999).
[5] K. Sokolowski-tinten, J. Bialkowski and D. Von Der Linde, Phys. Rev. B. 51, 14186–14198 (1995).
[6] H. M. Van Driel, Phys. Rev. B. 35, 8166 (1987).
[7] A. Rämer, O. Osmani and B. Rethfeld, J. Appl. Phys. 116, 53508 (2014).
[8] N. M. Bulgakova and A. V. Bulgakov, Appl. Phys. A. 73, 199–208 (2001).
[9] B. N. Chichkov, C. Momma, S. Nolte, F. von Alvensleben and A. Tuennermann, Appl. Phys. A. 63, 109–115 (1997).
[10] C. Momma, S. Nolte, B. N. Chichkov, F. V. Alvensleben and A. Tuennermann, Appl. Surf. Sci. 109–110, 15–19 (1997).
[11] C. Momma, B. N. Chichkov, S. Nolte, F. Von Alvensleben, A. Tuennermann, et al., Opt. Commun. 129, 134–142 (1996).
[12] P. S. Banks, M. D. Feit, A. M. Rubenchik, B. C. Stuart and M. D. Perry, Appl. Phys. A. 69, S377–S380 (1999).
[13] X. Liu, D. Du and G. Mourou, IEEE J. Quantum Electron. 10, 1706–1716 (1997).
[14] B. Neuenschwander, B. Jaeggi, M. Schmid, V. Rouffiange and P.-E. Martin, Proc. SPIE. 8243 (2012).
[15] S. Nolte, C. Momma, H. Jacobs, A. Tünnermann, B. N. Chichkov, et al., JOSA B 14, 2716–2722 (1997).
[16] N. Bärsch, K. Körber, A. Ostendorf and K. H. Tönshoff, Appl. Phys. A. 77, 237–242 (2003).
[17] P. Allenspacher, B. Hüttner and W. Riede, Proc. SPIE. 4932 (2003).
[18] P.P. Pronko, P. A. VanRompay, C. Horvath, F. Loesel, T. Juhasz, et al., Phys. Rev. B. 58(5), 2387–2390 (1998).
[19] J. Bonse, S. Baudach, J. Krüger, W. Kautek and M. Lenzner, Appl. Phys. A. 74, 19–25 (2002).
[20] G. J. Lee, Y. P. Lee, H. Cheong, C. S. Yoon, C. H. Oh, et al., J. Korean Phys. Soc. 48, 1268–1272 (2006).
[21] G. D. Tsibidis, M. Barberoglou, P. A. Loukakos, E. Stratakis and C. Fotakis, Phys. Rev. B. 86, 115316 (2012).
[22] J. Bonse, A. Rosenfeld and J. Krüger, J. Appl. Phys. 106, 104910 (2009).
[23] J. Bonse and J. Krüger, J. Appl. Phys. 108, 34903 (2010).

[24] J. Bonse, M. Munz and H. Sturm, J. Appl. Phys. 97, 13538 (2005).
[25] Z. Guosheng, P. M. Fauchet and A. E. Siegman, Phys. Rev. B. 26, 5366 (1982).
[26] S.I. Anisimov, N. A. Inogamov, Yu. V. Petrov, V. A. Khokhlov, V. V. Zhakhovskii, et al., Appl. Phys. A. 92, 939–943 (2008).
[27] S. I. Anisimov, B. L. Kapeliovich and T. L. Perelman, Soviet Phys. JETP. 39, 375 (1974).
[28] J. K. Chen, D. Y. Tzou and J. E. Beraun, Int. J. Heat Mass Transfer 48, 501–509 (2005).
[29] A. Kiselev, J. Roth and H. Trebin, High Performance Computing in Science and Engineering (Springer Heidelberg, 2016) pp. 189–202.
[30] S. I. Anisimov, V. V. Zhakhovskii, N. A. Inogamov, K. Nishihara, A. M. Oparin, et al., JETP Lett. 77, 606–610 (2003).
[31] B. Jaeggi, B. Neuenschwander, M. Schmid, M. Muralt, J. Zuercher, et al., Phys. Procedia 12, 164–171 (2011).
[32] B. Neuenschwander, G. F. Bucher, G. Hennig, C. Nussbaum, B. Joss, et al., Proc ICALEO, Anaheim, California (2010).
[33] M. Domke, G. Piredda, J. Zehetner and S. Stroj, J. Laser Micro Nanoeng. 11, 100 (2016).
[34] J. M. Liu, Opt. Lett. 7, 196 (1982).
[35] J. F. Reintjes and J. C. Mcgroddy, Phys. Rev. Lett. 30, 901 (1973).
[36] Y. Gan and J. K. Chen. Appl. Phys. A. 105, 427–437 (2011).
[37] E. D. Palik, in 'Handbook of Optical Constants of Solids'. (Academic Press, Boston, 1985).
[38] H.S. Sim, S. H. Lee and J. S. Lee, J. Mech. Sci. Technol. 21, 1847–1854 (2007).
[39] C. P. Grigoropoulos, R. H. Buckholz and G. A. Domoto, J. Appl. Phys. 60, 2304–2309 (1986).